

# Application of a Combined Optical–Passive Microwave Method to Retrieve Soil Moisture at Regional Scale Over Chile

Andrés Santamaría-Artigas, Cristian Mattar, and Jean-Pierre Wigneron, *Senior Member, IEEE*

**Abstract**—This work presents the calibration and evaluation of an optical–passive microwave method for retrieving soil moisture (SM) at regional scale using remote sensing and reanalysis data. Several data sets were used, such as the bipolarized brightness temperature provided by SM and Ocean Salinity (SMOS) L3 brightness temperature product, the Normalized Difference Vegetation Index (NDVI) from moderate resolution imaging spectroradiometer (MODIS), the soil temperature and water content of the first 0–7 cm of depth from the ERA-Interim reanalysis, and 13 land cover classes obtained from the ECOCLIMAP database. The method was applied over Chile between 28°S and 43°S for 2010–2012. The data set was used to calibrate and evaluate a semiempirical approach for estimating SM, first by using only the data from SMOS and ERA-Interim and then also including the MODIS vegetation indicator. Results were analyzed for every land cover class using the determination coefficient ( $r^2$ ), the coefficients obtained from the regressions, and the unbiased root-mean-square difference (ubRMSD). Results showed an increase in the average  $r^2$  for all classes when a vegetation index was used in the calibration of the approach. The increases in  $r^2$  ranged from 3% for the crop class, to 49% for the closed shrubland class. The ubRMSD presented a decrease in its value of up to 1%  $m^3/m^3$  for the woodlands, open shrublands, and woody shrublands classes and up to 2%  $m^3/m^3$  for the closed shrubland class. These results contribute to the use of single linear and semiempirical regressions to estimate SM at regional scale based on SMOS L-band bipolarized brightness temperature.

**Index Terms**—ERA-Interim, Moderate Resolution Imaging Spectroradiometer (MODIS), Normalized Difference Vegetation Index (NDVI), Soil Moisture and Ocean Salinity (SMOS), Soil Moisture (SM).

## I. INTRODUCTION

S OIL MOISTURE (SM) plays a key role in meteorological and hydrological forecasting as it determines the evaporation process between land surface and the atmosphere. Over

Manuscript received April 16, 2015; revised December 09, 2015; accepted December 11, 2015. Date of publication January 21, 2016; date of current version March 11, 2016. This work was supported in part by the FONDECYT-Iniciación (CONICYT/ref-11130359) and in part by the TOSCA (Terre Océan Surfaces Continentales et Atmosphère) CNES Programme at INRA-ISPA.

A. Santamaría-Artigas was with the Laboratory for Analysis of the Biosphere, Department of Environmental Sciences and Renewable Natural Resources, University of Chile, Santiago 1058, Chile. He is now with the Department of Geographical Sciences, University of Maryland, College Park, MD 20742 USA (e-mail: asantam@umd.edu).

C. Mattar is with the Laboratory for Analysis of the Biosphere, Department of Environmental Sciences and Renewable Natural Resources, University of Chile, Santiago 1058, Chile (e-mail: cmattar@uchile.cl).

J.-P. Wigneron is with the Institut National de Recherche Agronomique, Bordeaux 33140, France (e-mail: wigneron@bordeaux.inra.fr).

Color versions of one or more of the figures in this paper are available online at <http://ieeexplore.ieee.org>.

Digital Object Identifier 10.1109/JSTARS.2015.2512926

the last few decades, new technologies have been developed for performing SM estimates at different spatial and temporal scales. SM estimates can help determine the partitioning of precipitation into runoff, infiltration and surface storage, as well as the portioning of incoming solar radiation and long-wave radiation into outgoing long-wave radiation, latent heat flux, ground heat flux, and sensible heat flux [1]. Furthermore, SM maps at global or continental scales are crucial input for climate change studies [2], surface–atmosphere interactions [3], weather forecasting [4] and agriculture applications [5], among others. Therefore, the need for reliable SM information has motivated many scientists to generate SM estimates from land surface modeling, remote sensing techniques, or a combination of both through land data assimilation systems [6].

Above all other methods for estimating SM at global scale, the ones based on remote sensing techniques have experienced the most significant improvements in recent decades. In fact, a high number of studies have been conducted to obtain SM from spaceborne microwave instruments [7]–[9]. Microwave remote sensing is capable of providing quantitative information about the water content of a shallow near surface layer [10], particularly in the low-frequency microwave region from 1 to 10 GHz. For instance, the Scanning Multichannel Microwave Radiometer (SMMR) operated on Nimbus-7 between 1978 and 1987 (6.6 GHz and above) [11], the Special Sensor Microwave Imager (SSM/I), launched in 1987 (19 GHz and above) [12], the Advanced Microwave Scanning Radiometer-Earth (AMSR-E) observation system (on board on Aqua satellite working from 6.9 to 89 GHz) [8], Windsat (from 6.8 to 37 GHz) [13], the Advanced Scatterometer [14], and the scatterometer on board the European Remote Sensing Satellite (ERS-1 and 2, working at 5.3 GHz). At L-band (1.4 GHz), the SM in the first few centimeters of soil significantly impacts the measured brightness temperature in about 2 K per 1% of volumetric SM over bare soil [15], [16]. Moreover, L-band microwaves have the advantage of being insensitive to the effects of both clouds and the Earth's atmosphere [17]. Because of this, L-band radiometry has proven to be one of the most promising remote sensing techniques for monitoring SM over land surface at large scales [18].

Radiometric L-band satellite measurements were initially tested by the Skylab mission between January 1973 and July 1974 [19]. More recently, new passive satellite missions working on the L-band microwave range have been developed in order to improve the surface SM estimates and ocean salinity at global scale [17], [18], [20]. The most recent L-band mission

currently in orbit is the SM Active Passive (SMAP) mission [21] launched in January 2015. The SMAP mission was originally planned to combine radar and radiometer measurements in order to estimate SM; however, on July 2015, the radar stopped transmitting due to an anomaly that involved the radar's high power amplifier, and since then SMAP has continued to work with data from the radiometer only. Another recent *L*-Band mission is the SM and Ocean Salinity (SMOS) mission launched in November 2009, which was specially designed for monitoring SM by acquiring passive microwave data at a suitable frequency for SM retrieval, providing global maps of SM every three days at a nominal spatial resolution better than 43 km with an accuracy goal of  $0.04 \text{ m}^3/\text{m}^3$  [22].

The SMOS surface SM data are generated by the SMOS Level-2 algorithm. These routines are an iterative approach that aims to minimize a cost function whose main component is the sum of the squared weighted differences between measured and modeled TB data for a collection of incidence angles [18]. The measured TB is obtained by SMOS and the upwelling set of TB values is simulated using the *L*-band Microwave Emission of the Biosphere Model (L-MEB) [23]. The L-MEB model uses the tau-omega ( $\tau\text{-}\omega$ ) microwave emission model previously calibrated over a wide range of land covers defined in the ECOCLIMAP database [24].

In the  $\tau\text{-}\omega$  model, the optical depth of the vegetation layer ( $\tau$ ) is physically related to its water content [19] or Leaf Area Index (LAI) [25], and the vegetation single scatter albedo ( $\omega$ ) is neglected or parameterized for site-dependent cases. Recent works have demonstrated the high correlation between  $\tau$  and optical/near infrared vegetation indices such as the Normalized Difference Vegetation Index (NDVI) or the Enhanced Vegetation Index (EVI) [26]. The  $\tau\text{-}\omega$  approach has been tested over several land cover at *in situ* and global scales, considering the vegetation parameter as an indicator of the vegetation optical depth [23], [25]–[28]. These optical/IR vegetation indices can be derived from *in situ* observations and remote sensing data. For instance, geostationary data from sensors such as the one on the Geostationary Operational Environmental Satellite (GOES), or the Spinning Enhanced Visible and Infrared Imager (SEVIRI) on the METEOSAT Second Generation Satellite (MSG), and data from polar orbit sensors such as Landsat 7 Enhanced Thematic Mapper Plus (ETM+), Landsat 8 Operational Land Imager (OLI), the moderate resolution imaging spectroradiometer (MODIS) on board the TERRA and AQUA, and the Advanced Very High Resolution Radiometer (AVHRR) on board the National Oceanic and Atmospheric Administration (NOAA) platforms.

One approach that considers vegetation indices in the  $\tau\text{-}\omega$  model was proposed in [28] and uses the NDVI as an indicator of  $\tau$ . However, this approach has only been tested with *in situ* data from the SMOSREX site [29], and an evaluation of the model over regional scales has not yet been performed. Although several studies have demonstrated the potential of other vegetation indices at local and regional scales [26], [27], [30], the use of a semiempirical approach to estimate SM at regional scale is necessary in order to test its performance at and also to quantify the impact of a vegetation index in its respective calibration and evaluation of retrievals. Therefore, the aim of

this work is to analyze SM retrieved at regional scales, from an originally *in situ* derived optical–passive microwave semiempirical approach, by using remote sensing and reanalysis data from central and southern Chile. The structure of this work is detailed as follows. Section II presents the study area and data used. Section III shows the method used to calibrate and evaluate the model over central and southern Chile, results of which are presented in Section IV. Finally, Section V presents the discussion and conclusion of this work.

## II. STUDY AREA AND DATA ACQUISITION

### A. Chilean Central Zone

The study area is located between  $28^\circ$ – $43.5^\circ$  S and  $69.5^\circ$ – $74.5^\circ$  W. Within the study area, three zones with distinct land cover and climatic characteristics were defined. In the northern zone, the predominant climatic conditions are of a semiarid type, and it is mostly covered by sparse vegetation and shrublands. The central zone, which is the country's most agriculturally productive zone, is covered by several types of crops, forests, and bare soil areas, and has warm-summer Mediterranean climatic conditions. Finally, the southern zone is mostly covered by forests and grasslands, and has temperate and oceanic climatic conditions. Fig. 1 shows the study area and selected climatic diagrams that illustrate the range of precipitation and average temperatures.

### B. Data

Different sources of data were used for the calibration and evaluation of the optical–passive microwave semiempirical approach (Table I). The data used in this work cover the period between January 1, 2010 and December 31, 2012, and is detailed in the following.

1) *Moderate Resolution Imaging Spectroradiometer*: The MOD13Q1 V5 Vegetation Index product [31] was used as a vegetation indicator. This product includes the 16-day composite NDVI determined from red and near-infrared reflectance values at a spatial resolution of 0.25 km. The product is generated using the maximum value compositing (MVC) technique, in which the highest NDVI value from a 16-day time window is selected for every pixel in order to reduce the presence of cloud contaminated or atmospherically affected observations.

2) *SM and Ocean Salinity*: Vertically and horizontally polarized *L*-band brightness temperatures at  $42.5^\circ$  were obtained from SMOS Level-3 data at both ascending and descending orbits. The SMOS L3 Brightness Temperature daily product (TBL3) delivers global *L*-Band brightness temperatures at a resolution of 25 km and at different viewing angles [18]. For this work, the SMOS L3 RE02 version delivered in the Equal-Area Scalable Earth Grid [32] was used. Since the calibration of the optical–passive microwave semiempirical approach depends on SMOS brightness temperature, it was decided not to use the SMOS SM product, as the intercomparison of SM derived from dependent data sets could generate an autoregressive problem.

## LIST OF FIGURES

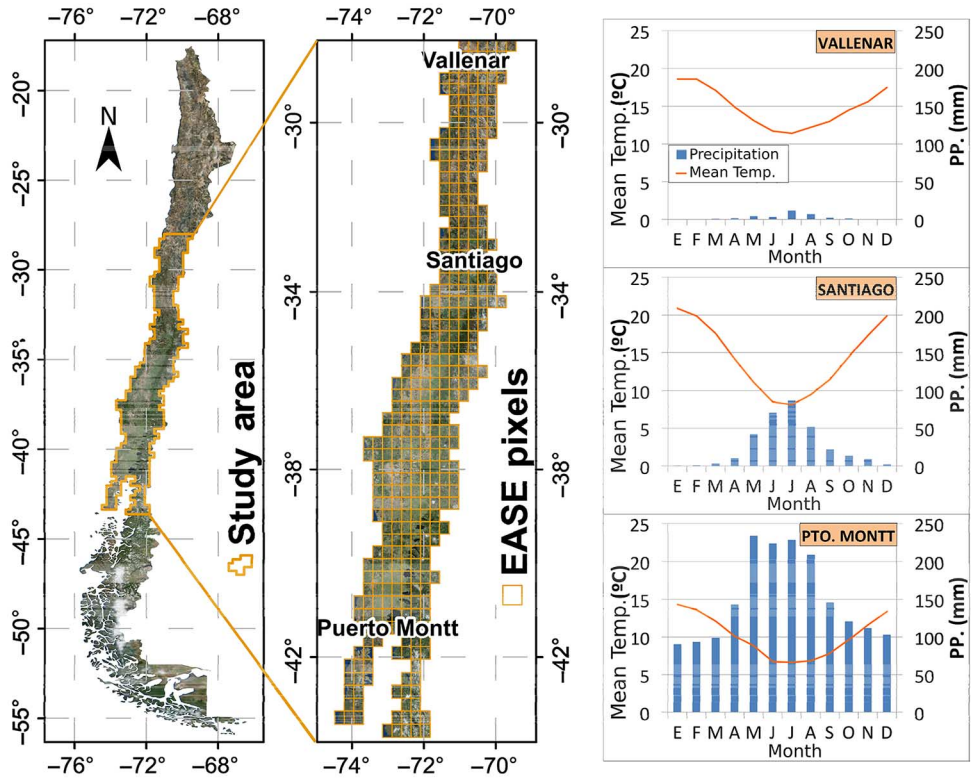
Fig. 1. Study area and 25-km<sup>2</sup> pixels used in this work. The climatic diagrams show the range of precipitation and mean temperature in the study area.

TABLE I  
LIST OF DATA SETS USED

Parameter	Product	Source	Spatial Resolution	Temporal Resolution	Time Period
Brightness temperature at 42.5° (H, V)	L3TB	SMOS	25 km	Daily	
Normalized Difference Vegetation Index	MOD13Q1	MODIS	0.25 km	16 days composite	
Soil Temperature (0 – 7 cm)	STL1	ERA Interim	0.125 °		01/01/2010 - 31/12/2012
Soil Moisture (0 – 7 cm)	SWVL1			3 hours	

3) *ERA Interim*: The ERA-Interim reanalysis produced by the European Centre for Medium-Range Weather Forecasts (ECMWF) is a reliable source of meteorological data for scientific research and development [33]. ERA-Interim data are available from 1979 to present day and includes global meteorological data at different temporal and spatial resolutions. For this work, two different ERA-Interim products were used: 1) the STL1 soil temperature at the first layer of depth (0–7 cm) product and 2) the VSWL1 volumetric soil water layer 1 (i.e., the water content between the surface and the first 7 cm of soil) product. Both data sets have a spatial resolution of  $0.125^\circ \times 0.125^\circ$  and a temporal resolution of 3 h. Several works have compared SM estimates from microwave remote sensing and *in situ* observations, demonstrating the quality of ERA-Interim SM products [6], [34], [35].

4) *ECOCLIMAP*: The ECOCLIMAP database [24] was generated from previously available land cover maps, climatic data, and information from AVHRR, and delivers global land cover maps of 215 classes defined by areas of homogeneous vegetation at a spatial resolution of  $1 \text{ km} \times 1 \text{ km}$  [36]. The

ECOCLIMAP database is used in the SMOS L2 SM retrieval algorithm, and so it was selected to test the performance of the semiempirical approach per land cover class. Classes analyzed in this work are: Crops (C.), closed shrubland (C. S.), deciduous forest (D. F.), evergreen forest (E. F.), grasslands (G.), mixed forest (M. F.), open shrubland (O. S.), rocks (R.), woodlands (W.), and woody shrubland (W. S.).

## III. METHOD

A. *Semiempirical Method*

The semiempirical regressions used in this work are based on the  $\tau\omega$  model applied over vegetation covers [37]. The *p*-polarized brightness temperature  $T_b(\theta, p)$  is written as a function of the single scattering albedo  $\omega(\theta, p)$ , the vegetation optical depth  $\tau(\theta, p)$ , the soil reflectivity  $\Gamma_S(\theta, p)$ , the downward atmospheric and galactic brightness temperatures  $T_{b_\theta}^{SKY\downarrow}$ , and the soil  $T_S^E$  and vegetation  $T_V^E$  effective temperatures as in the following equation:

$$\begin{aligned} Tb(\theta, p) = & (1 - \omega)(1 - \gamma)(1 - \gamma\Gamma_S(\theta, p))T_V^E \\ & + \gamma(1 - \Gamma_S(\theta, p))T_S^E + Tb_\theta^{SKY\downarrow}\Gamma_S(\theta, p)\gamma^2 \end{aligned} \quad (1)$$

where  $\gamma = \gamma(\theta, p)$  is the  $p$ -polarized transmissivity of the vegetation layer, which can be expressed as a function of the optical depth, and the incidence angle  $\theta$  as in the following equation:

$$\gamma(\theta, p) = \exp\left(-\frac{\tau(\theta, p)}{\cos(\theta)}\right). \quad (2)$$

Some simplification, such as considering the effective soil and vegetation temperatures as equal ( $T_S^E = T_V^E = T_C$ ) [38] and neglecting the effects of the upward and downward atmospheric emission [39], can be introduced without inducing significant errors.

Reference [39] initially developed a semiempirical approach assuming that the single-scattering albedo effects can be neglected, which is generally a good approximation for  $L$ -band [40]. It is important to note, however, that as the vegetation constituents approach lengths similar or larger than the used wavelengths (such as trees and stem-dominated agricultural vegetation), the effects of the scattering albedo become more significant [41]–[43]. With this in mind, (1) can be written as the following:

$$Tb(\theta, p) = T_C(1 - \Gamma_S(\theta, p)\gamma^2). \quad (3)$$

The surface emissivity  $e(\theta, p)$ , which is defined as  $e(\theta, p) = Tb(\theta, p)/T_C$  can be written the following:

$$e(\theta, p) = 1 - \Gamma_S(\theta, p)\gamma^2. \quad (4)$$

Soil reflectivity can be assumed to be proportional to surface SM ( $w_S$ ) according to the following equation:

$$\Gamma_S(\theta, p) \cong Ap(\theta)w_S \quad (5)$$

where  $w_S$  is the SM and  $Ap(\theta)$  is a site-dependent coefficient that implicitly accounts for the sensor configuration and all the soil characteristics that determine soil emission: mainly soil texture, structure and surface roughness, among others. Thus, by replacing (5) in (3), the SM can be written as a function of the vegetation optical thickness, surface effective temperatures, and bipolarized brightness temperature. Reference [39] tested (5) over barren areas. However, [28] adapted this approach for a vegetated area including a vegetation indicator as described in the following equation:

$$\begin{aligned} \log(w_S) = & a + b(\ln(1 - \Gamma(\theta, H))) + c(\ln(1 - \Gamma(\theta, V))) \\ & + d * Veg \end{aligned} \quad (6)$$

where  $a$ ,  $b$ ,  $c$ , and  $d$  are the regression coefficients,  $\Gamma$  is the horizontally ( $H$ ) and vertically ( $V$ ) polarized  $L$ -band microwave reflectivity defined as  $\Gamma = 1 - (Tb/T_C)$ , where  $Tb$  and  $T_C$  are the  $L$ -band brightness temperature and the effective temperature, respectively, and  $Veg$  is a surface vegetation indicator. So, (6) can be rewritten as

$$\begin{aligned} \log(w_S) = & a\left(\log\left(1 - \frac{Tb(\theta, H)}{T_C}\right)\right) \\ & + b\left(\log\left(1 - \frac{Tb(\theta, V)}{T_C}\right)\right) + c(Veg) + d. \end{aligned} \quad (7)$$

Equation (7) was tested over the SMOSREX site by [29] using the NDVI as a vegetation indicator and obtained significantly improved results in SM estimation. The SMOSREX site features an  $L$ -band multiangular bipolarized field radiometer [44], *in situ* SM and temperature sensors at several soil depths, a near-infrared radiometer, and other meteorological instruments installed for monitoring other biophysical parameters.

## B. Data Processing

The ERA-Interim VSWL1 and STL1 products, and the NDVI from MODIS were resampled to the spatial resolution of the SMOS pixels ( $25 \times 25$  km) using an averaging filter. In order to maintain the correct classification of the ECOCLIMAP data set, a majority filter was used to obtain the values of the new pixels instead. With the resampled data, a time series between January 2010 and December 2012 of TB, VSWL1, STL1, and NDVI was generated for each pixel of the study area. In order to match the SMOS TB data to the rest of the observations, those closest to the SMOS overpass time were selected.

The SMOS TB data were then filtered from the data set using the polarization ratio index defined as  $PR = (Tb(V) - Tb(H)) / (Tb(V) + Tb(H))$ , where  $Tb(V)$  and  $Tb(H)$  are the vertically and horizontally polarized brightness temperatures. The PR index allows to identify anomalies in the microwave signal, such as those produced by frozen soil [29], water intercepted in the vegetation [45], and  $Tb(H)$  values greater than  $Tb(V)$  values [28]. In this work, data points with a PR index lower than 0.02 were filtered out as in [28] and [45].

## C. Calibration and Evaluation (CAL/EVAL) of the Semiempirical Approach

Using the filtered data series, a statistical calibration process was carried out to obtain the regression ( $a$ ,  $b$ ,  $c$ , and  $d$ ) and determination ( $r^2$ ) coefficients between SM, TB, ST, and NDVI. In order to test for the effects of the NDVI on the approach, (7) was the first calibrated setting  $VEG = 0$  ( $SM_{(VEG=0)}$ ) to only consider the TB and ST as predictors of SM. Next, the  $VEG$  predictor was set equal to the NDVI from MODIS ( $SM_{(VEG=NDVI)}$ ), and a new set of correlation and calibration coefficients was obtained. The two set of coefficients ( $VEG = 0$  and  $VEG = NDVI$ ) were then compared to evaluate if the inclusion of remotely sensed NDVI improved the calibration of the approach. This procedure was carried out independently for 2010–2012 and analyzed by land cover class.

The evaluation of the SM retrievals consisted on the comparison of the estimates obtained ( $SM_{(VEG=0)}$  and  $SM_{(VEG=NDVI)}$ ) for each independent year against the SM product provided by ERA. The magnitude of the improvements was evaluated using both the determination coefficient ( $r^2$ ), and the unbiased root-mean-square difference (ubRMSD) defined as  $\sigma^2$ , where  $\sigma$  is

the standard deviation of the differences between the estimated and the observed values [46]. The ubRMSD metric was selected because it is not compromised by biases that might exist in the mean or by the amplitude of fluctuations in the retrieval [47]. The evaluation was carried using the data from the years, which are not considered in the calibration and for each of the land cover classes.

#### IV. RESULTS

##### A. Data Processing

The land cover classes obtained after the aggregation of the original ECOCLIMAP classes, along with the mean and standard deviation of NDVI for the whole data period are shown in Fig. 2. The NDVI did not show any strong variation during the period used to calibrate or evaluate the semiempirical method. Besides from some outliers located on the coastline of Chile, the remainder of pixels exhibits a low temporal variation. The magnitude of the NDVI follows the latitudinal gradient between semiarid conditions to the rainforest climate, with values ranging from almost 0.0 to 0.9.

With regard to the aggregation of the ECOCLIMAP data, results showed that in the northern zone of the study area, the most common classes are open and closed shrublands; for the central zone, the main classes are woody grasslands, woodlands, and evergreen needleleaf forests, along with a few cropland pixels and a single urban class pixel that corresponds to the city of Santiago. Finally, the main classes left in the southern zone after the aggregation method are mixed forest, evergreen needleleaf forest, and deciduous broadleaf forests, along with a few inland water pixels that correspond to lakes present in this zone.

The total and filtered data points available for each one of the land cover classes by calibration and evaluation year are shown in Table II. This table presents the high influences of the selection criteria over the land cover classes. The proportion between the total and filtered data for each year is equivalent, although there are some land cover classes in which the valid data points show an important reduction, such as evergreen forest or open shrublands, which might be explained by the effects of snow cover or by the SMOS quality flags.

##### B. Calibration

*1) Determination Coefficient:* The spatial distribution of the determination coefficients obtained by the regressions in which the vegetation indicator was set equal to zero and by those that included the NDVI from MODIS is shown in Fig. 3.

The use of NDVI seems to improve the obtained  $r^2$  from the statistical calibrations for each pixel between 8% and 20%, depending on the land cover (Fig. 4). On average, the improvements when using the NDVI in terms of  $r^2$  for the calibration of the method are 23% for the northern zone of the study area, which is mainly covered by open, closed, and woody shrublands. The central zone, covered by woody shrublands, crops, and evergreen forests, showed an average improvement of 10%. Finally, for the southern zone of the study area covered by different forest classes, the average improvement was 8%.

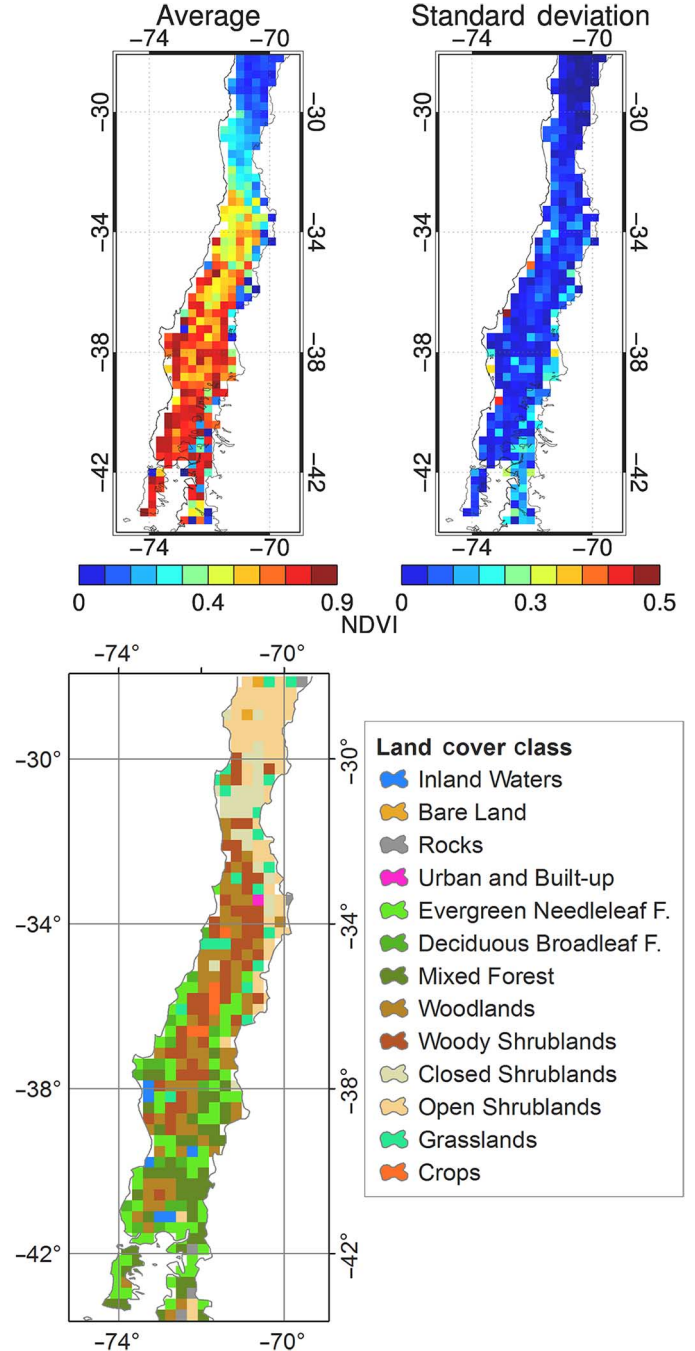


Fig. 2. Mean NDVI with standard deviation over the data period (2010–2012), and ECOCLIMAP classes after aggregation to  $25 \text{ km} \times 25 \text{ km}$ .

Similar results were obtained for single years (not shown), which suggests a high improvement in  $r^2$  for all classes when the NDVI from MODIS is included in the calibration of (7). In fact, for every land cover class of the study area, the  $r^2$  increased when the NDVI from MODIS was considered in the semiempirical method. For calibration year 2010, the woodland, evergreen, deciduous, and mixed forest classes showed an average increase in the  $r^2$  of 13%, 10%, 7%, and 10%, respectively. In the case of crops and grasslands classes, the average  $r^2$  increase was 3% and 14%, respectively. As for the closed, open, and woody shrubland classes, the average  $r^2$  increase was

TABLE II  
NUMBER OF TOTAL AND VALID DATA POINTS BY YEAR AND LAND COVER CLASS

Land cover class	2010		2011		2012	
	Total	Filtered	Total	Filtered	Total	Filtered
Woodlands	20579	12053	28554	15872	27982	16014
Evergreen Forest	19053	6981	26232	9009	25779	9073
Deciduous Forest	4787	2403	6674	3292	6553	3186
Mixed Forest	16514	8461	22734	10692	22337	11013
Crops	1533	1261	2392	1978	2358	1944
Grasslands	5619	2230	7694	2922	7599	2973
Open Shrublands	17067	5455	23395	7447	23167	7557
Closed Shrublands	7411	3646	10199	4892	10084	4898
Woody Shrublands	16233	10157	22621	13541	22157	13304
Rocks	1508	301	2082	396	2048	392

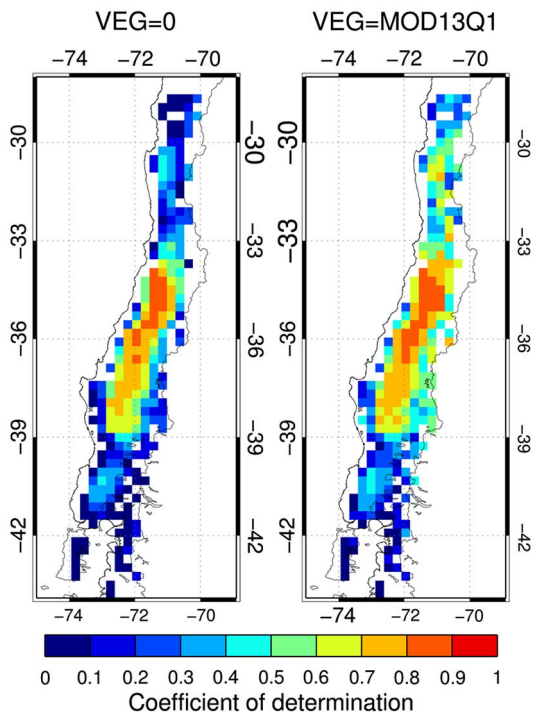


Fig. 3. Spatial distribution of the mean determination coefficient obtained from the calibration of the semiempirical approach when setting VEG = 0 and VEG = MOD13Q1.

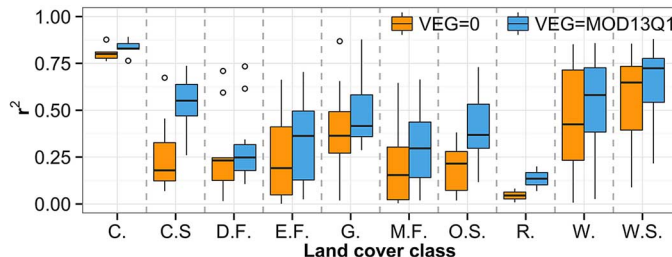


Fig. 4. Mean coefficient of determination boxplots for the regressions using VEG = 0 and VEG = MOD13Q1. Outliers are shown as circles.

estimated at 30%, 49%, and 15%, respectively. The rock classes showed an average increase of 5%. During calibration year 2011, the woodland, evergreen, deciduous, and mixed forest classes showed an increase in the average  $r^2$  of 10%, 18%, 5%, and 11%, respectively. For the crops and grassland classes, the average  $r^2$  increase was 3% and 4%, respectively. The closed, open, and woody shrubland classes presented an average  $r^2$  increase of 19%, 28%, and 10%, respectively. The rock classes showed an average increase of 6%.

Finally, for calibration year 2012, the woodland, evergreen, deciduous, and mixed forest classes showed an increase in the average  $r^2$  of 7%, 6%, 4%, and 9%, respectively. In the case of crops and grasslands classes, the average  $r^2$  increase was 3% and 12%, respectively. As for the closed, open, and woody shrubland classes, the average  $r^2$  increase was 16%, 15%, and 7%, respectively. The rock classes showed an average increase of 15%.

2) *Regression Coefficients:* The spatial distribution of the coefficients obtained from the regressions that did not include the NDVI (VEG = 0) and those that considered the NDVI from MODIS (VEG = NDVI) are shown in Fig. 5.

Coefficients “a” and “b” [coefficients associated with TB(H) and TB(V), respectively] do not show differences in their spatial pattern when the NDVI from MODIS was included in the calibration of the semiempirical approach. However, a decrease in the magnitude of both coefficients can be observed. As for coefficient “c” (NDVI), no high spatial differences between the three calibration years were observed, despite some isolated cases in the northern area. Coefficient “d” showed the highest changes in its spatial pattern when the NDVI was considered in the calibration, especially in the central area.

The boxplots of the regression coefficients by land cover class are shown in Fig. 6. The magnitude of coefficient “a” decreased for land cover class when the NDVI from MODIS was used in the semiempirical approach. The highest range in the coefficient “a” values for every calibration year was shown by the open shrubland classes. This result might be explained by the heterogeneous spatial distribution of this class, which has pixels from the coast all the way up to the Andes mountain range. Coefficient “b” did not show strong differences in magnitude between the regressions that did not consider a vegetation index and those that considered the NDVI from MODIS. This could be attributed to the interaction between the vertically polarized signal and the vertical structure of each land cover class [39], which in the case of crops can vary depending on the species and agricultural management. Coefficient “c” showed the highest magnitudes of all the coefficients. For the three calibration years, the “c” coefficient maintained a similar range by land cover class, which was greater in the shrubland classes. This effect on the NDVI coefficient can be attributed to the heterogeneous spatial distribution of these land cover classes. All classes showed an increase in the range of coefficient “d” when the NDVI was included in the calibration of the semiempirical approach. The magnitude of coefficient “d” by land cover class held steady for all the calibration years, showing the lowest values in the open and closed shrubland classes.

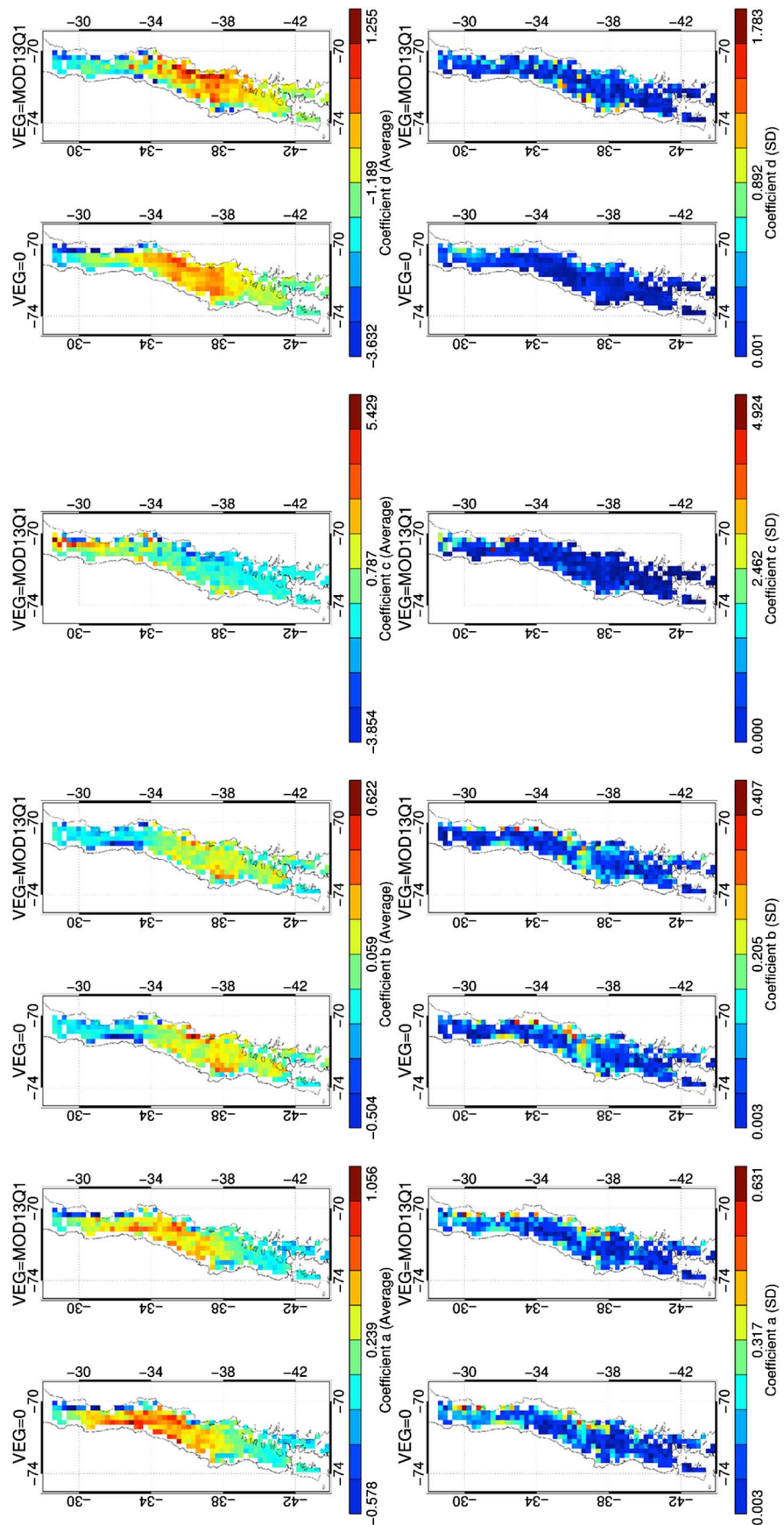


Fig. 5. Spatial distribution of mean regression coefficients (top row) with standard deviation (bottom row).

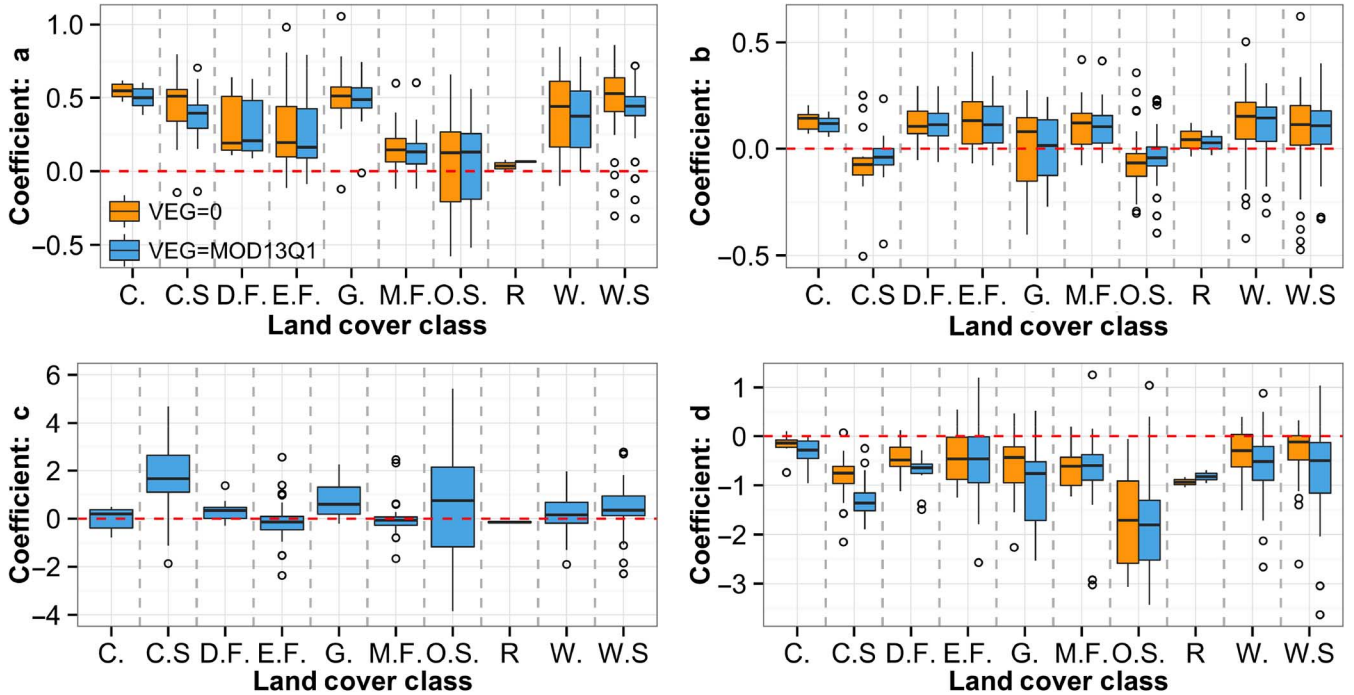


Fig. 6. Boxplots of averaged coefficients. (a) Top-left, (b) top-right, (c) bottom-left, and (d) bottom-right of the regressions with  $\text{VEG} = 0$  and  $\text{VEG} = \text{MOD13Q1}$  by land cover class. Outliers are shown as circles and the red dotted line shows the 0 value.

### C. Evaluation

1) *Determination Coefficient*: The  $r^2$  of the evaluation also showed an improvement when the NDVI from MODIS was included in the approach in comparison to when VEG was set equal to zero (Fig. 7). This is noticed for several land cover classes, such as closed shrublands, evergreen needleleaf forest, mixed forest, open shrubland, and rocks. The rest of the land cover classes also show a slight improvement when using the NDVI from MODIS, although it is not statistically significant ( $p < 0.05$ ). Furthermore, for classes such as grasslands, woodlands or woody shrublands, the minimum limit of the boxplot is higher when using the NDVI, though similar values were obtained in the maximum limit. The rock class displays an unusual behavior, which might be attributed to its location in the Andes Mountains, where the seasonal rainfall can generate a low vegetation cover. In the case of crops, the phenological stage cannot be evidenced in the aggregated pixels and therefore mixed information from the NDVI can affect the semiempirical approach in terms of its  $r^2$ .

2) *Unbiased Root-Mean-Square Difference*: The ubRMSD obtained between the reference SM values and the SM estimates calculated using the coefficients from the regressions with  $\text{VEG} = 0$  and  $\text{VEG} = \text{MOD13Q1}$  by land cover class are shown in Fig. 8. Results show that if the NDVI from MODIS is included in the calibration of the semiempirical approach, the ubRMSD decreases by up to  $0.01 \text{ m}^3/\text{m}^3$  for the woodlands, open shrubland, and woody shrubland classes and up to  $0.02 \text{ m}^3/\text{m}^3$  for the closed shrubland classes.

These results are significant and similar to the improvements obtained in [28] at *in situ* level. The rest of the land cover

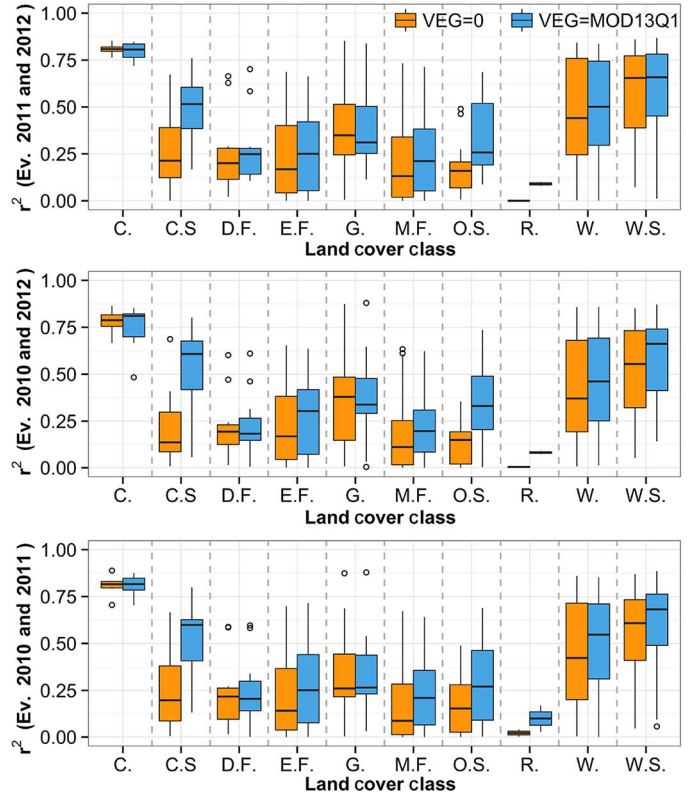


Fig. 7. Boxplots of mean coefficient of determination obtained between the SM reference values from ERA-Interim and the SM estimates using  $\text{VEG} = 0$  and  $\text{VEG} = \text{MOD13Q1}$  by land cover class for calibration year 2010 (evaluation years 2011 and 2012), 2011 (evaluation years 2010 and 2012), and 2012 (evaluation years 2010 and 2011). Outliers are shown as circles.

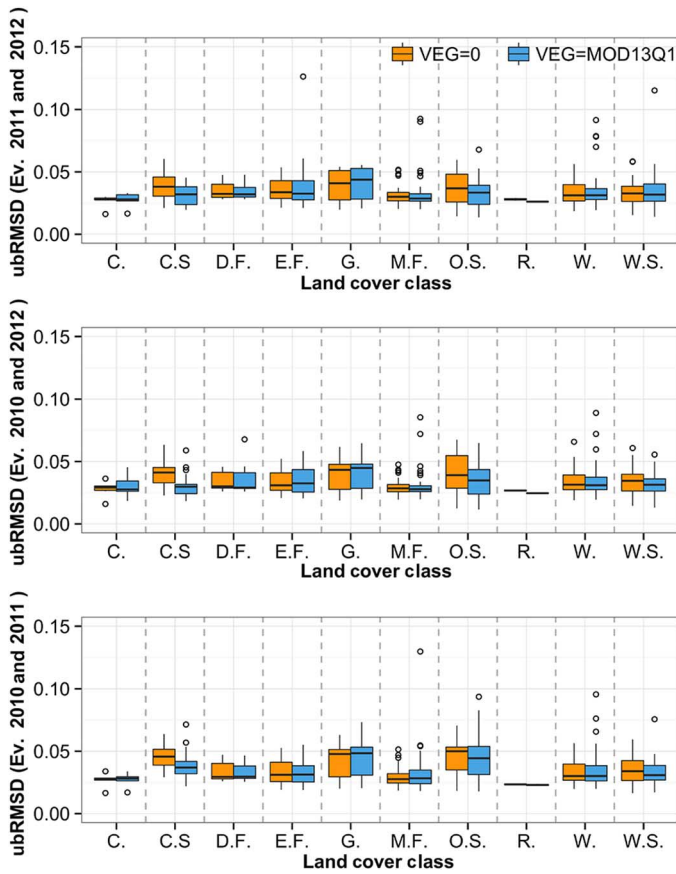


Fig. 8. Boxplots of ubRMSD obtained between the SM reference values from ERA-Interim and the SM estimates using  $VEG = 0$  and  $VEG = MOD13Q$  by land cover class. For calibration year 2010 (evaluation years 2011 and 2012), 2011 (evaluation years 2010 and 2012), and 2012 (evaluation years 2010 and 2011). Outliers are shown as circles.

classes also show a decrease in the ubRMSD magnitude when the NDVI from MODIS was included in the semiempirical approach; however, these decreases were less than  $0.01 \text{ m}^3/\text{m}^3$ . On the other hand, the mixed forest class exhibited pixels in which the ubRMSD increased by up to  $0.01 \text{ m}^3/\text{m}^3$  when the NDVI was included in the semiempirical approach, which could be explained by the heterogeneous spatial distribution of this class. Despite the fact that the use of NDVI improves the calibration in terms of  $r^2$ , the magnitude of these improvements is not necessarily related to the obtained ubRMSD, since the vegetation phenological stage could influence the SM estimations.

3) Time Series: To evidence the behavior of SM estimated by setting  $VEG = 0$  and  $VEG = MOD13Q1$ , Figs. 9 and 10 show the SM estimation for two different land cover classes. Fig. 9 shows a closed shrubland class pixel time series with the temporal behavior of SM estimated without using a vegetation index in the calibration of the semiempirical approach, and using the NDVI from MODIS. The temporal series shows that SM estimated using the NDVI has a temporal pattern similar to that of the reference SM given by the ERA-Interim VSWL1 product. The SM values exhibit a similar behavior in the case of extreme values (i.e., those related to precipitation events) and it is possible to characterize a dry and wet period related to the minimum and maximum NDVI values.

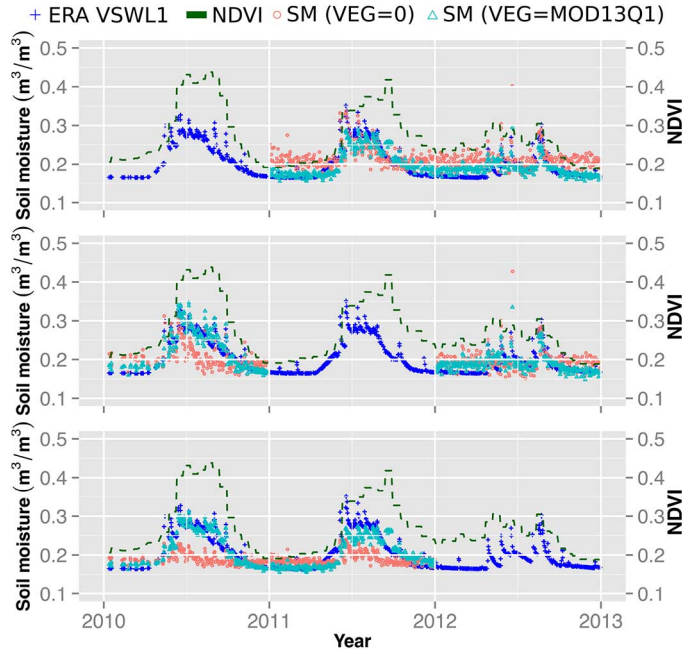


Fig. 9. Time series of SM and NDVI for calibration years 2010 (top), 2011 (middle), and 2012 (bottom). The time series belongs to a closed shrubland pixel located in coordinates  $30^{\circ}54'57.04''\text{S}$  and  $71^{\circ}1'25.86''\text{O}$ .

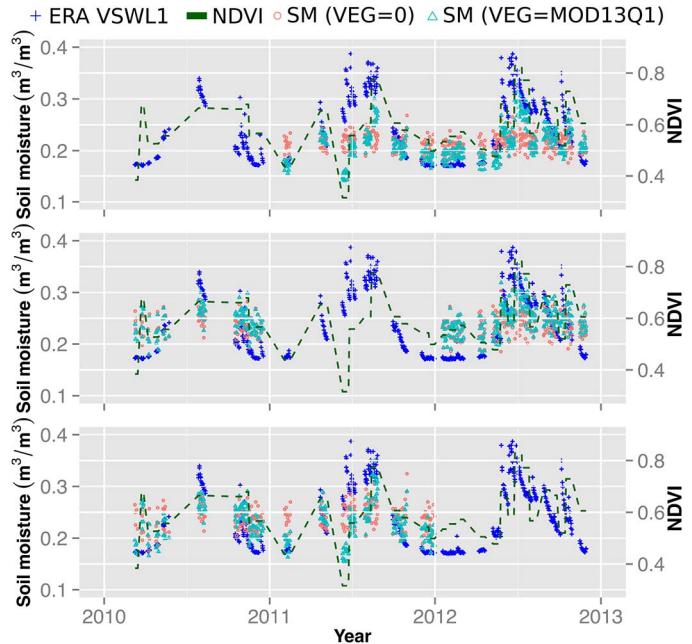


Fig. 10. Time series of SM and NDVI for calibration years 2010 (top), 2011 (middle), and 2012 (bottom). The time series belongs to a woodland pixel located in coordinates  $34^{\circ}53'31.18''\text{S}$ ,  $72^{\circ}5'2.96''\text{O}$ .

For 2012, a decrease in NDVI magnitude is evidenced which could be related to a decrease in rainfall; although this decrease did not influence the SM retrievals for 2010 and 2011 NDVI-based approach. Indeed, the best correlation was obtained when comparing ERA-Interim VSWL1 to SM( $VEG = MOD13Q1$ ), noticing a wet/dry season also related with the magnitude of the NDVI for those years.

On the other hand, Fig. 10 shows the temporal behavior of a woodland pixel. Even though the use of NDVI in the semiempirical approach slightly improved the SM estimates in comparison to when no vegetation index was considered, in extreme cases (mid of 2011), it is possible to see that the use of NDVI in the semiempirical approach might not improve the quality of the SM estimates. In this specific case, an event of unusually low NDVI shown in the Woodland time series could be produced by a particularly cloudy period which could not be excluded by the 16-day time composite product.

## V. DISCUSSION AND CONCLUSION

The use of NDVI in the calibration of the semiempirical approach significantly improves the SM estimates for some of the land cover classes of the study area. This application shows that the approach proposed in [28] can be applied to regional scales and it is a contribution to the interaction between data from different sources such as *L*-band microwaves, information from the optical range, and data from reanalysis. Previously, [30] showed the usefulness of semiempirical methods for the estimation of SM using different data sources; however, those estimates were made only over a single pixel. Moreover, this work presents the improvements in the calibration and evaluation of the semiempirical approach not only at regional scale, but also over different land cover classes.

In [28], the NDVI was compared with the LAI. Parrens *et al.* [27] showed that there was a significant improvement in the calibration and evaluation of the semiempirical method when the LAI was included as a vegetation indicator. Nevertheless, one of the most significant differences between the NDVI and LAI is related to the method used to estimate each vegetation indicator. Whereas NDVI is the same algorithm for every red and NIR band, the LAI can change according to the kind of sensor and algorithm proposed [48], [49]. This could introduce an additional source of uncertainty related to the estimation of the vegetation indicator and not to the semiempirical approach by itself.

For this work, two polarizations and one observation angle were considered for the brightness temperature data. Previous works have tested multiangularity as an additional source of information for semiempirical methods [25], [28], [39]. However, in order to consider the maximum amount of data possible for calibration and evaluation of the semiempirical approach, only information at 42.5° was considered in this work.

Regarding the land cover class, the ECOCLIMAP data base has been previously used in studies related to the estimation of SM at different spatial resolutions [26], [50]–[52]. However, some slight discrepancies occurred between the actual land cover classes in Chile and the ones in the ECOCLIMAP data base. Nevertheless, it is also important to note that the homogenization of land cover classes to a specific study area is a complex work that demands a more detailed analysis. This is shown by previous studies related to the discrepancies of several land cover databases and *in situ* validation [53]. The use of different global land cover classes to analyze SM retrievals

is still a challenge and future works will account for the use of land cover classes from updated or local data base instead of global thematic land cover classes.

The calibration of the algorithm was carried out by taking into account information from different soil depths, such as brightness temperature from SMOS (0–4 cm), vegetation index (surface), and SM and temperature from reanalysis (0–7 cm). However, the SM retrieved by the semiempirical approach was obtained for 0–7 cm, since the ERA-Interim SM product used for the calibration is modeled at this soil depth. However, the representativeness of the soil depth can change following the SM data used in the calibration. This is the key for further application at regional or global scale where the soil depth can influence the SM retrievals for the evaluation or even the validation procedures. Moreover, it is necessary to account that if the differences in soil depths are considered, SMOS and ERA-Interim SM values can be compared, but not quantitatively evaluated because the soil water content might be different.

In terms of calibration and evaluation year, the methodology proposed in this manuscript is consistent in terms of the statistical coefficients obtained to estimate SM at regional scale. The spatialized coefficients did not present significant differences between the calibration years, which seem to be consistent for the calibration over a wide range of land covers or for global scale. The calibration of this coefficient can be assimilated to obtain an operational routine for SM retrievals for regional to global scale and also for different land cover types.

The combined optical–passive microwave approach has been tested by using remote sensing and reanalysis data. The evaluation of the semiempirical approach by the analysis of the  $r^2$  showed that all the studied land cover classes had improvements in the SM estimation when the NDVI from MODIS was included as a vegetation indicator in the semiempirical approach. The land cover classes that showed the highest improvements when the NDVI was included in the approach were the open and closed shrubland classes with an improvement of 49% and 30%, respectively. These results are in accordance with the ones found by the analysis of the ubRMSD, in which the biggest improvements were obtained by the same land cover classes.

The results obtained in this work suggest that for certain land cover classes, the analyzed semiempirical approach can improve the SM estimates by up to  $0.02 \text{ m}^3/\text{m}^3$ . This approach, applicable to other spatial scales, might also be a useful resource for other spatial missions, such as SMAP launched in January 2015. Finally, it is important to note that the estimation of SM values from the semiempirical optical–passive microwave synergic approach allows for the generation of new sources of information concerning one of the earth's most crucial variables.

## ACKNOWLEDGMENT

The authors would like to thank CATDS for the SMOS L3 products, ECMWF for the ERA-Interim products, the MODIS team for the land surface products, and CNRM-GAME for the ECOCLIMAP database.

## REFERENCES

- [1] J. A. Sobrino, C. Mattar, B. Franch, J. C. Jiménez-Muñoz, and C. Corbari, "On the synergy between optical and TIR observation for retrievals of soil moisture content: Exploring different approaches," in *Remote Sensing of Energy Fluxes and Soil Moisture Content*, G. P. Petropoulos, Ed. Boca Raton, FL, USA: CRC Press, 2013, pp. 363–390.
- [2] H. Douville and F. Chauvin, "Relevance of soil moisture for seasonal climate predictions: A preliminary study," *Clim. Dyn.*, vol. 16, nos. 10–11, pp. 719–736, 2000.
- [3] R. D. Koster *et al.*, "Regions of strong coupling between soil moisture and precipitation," *Science*, vol. 305, no. 5687, pp. 1138–1140, 2004.
- [4] M. Drusch, "Initializing numerical weather prediction models with satellite-derived surface soil moisture: Data assimilation experiments with ECMWF's integrated forecast system and the TMI soil moisture data set," *J. Geophys. Res.*, vol. 112, no. 3, pp. 1–14, 2007.
- [5] D. W. Shin, J. G. Bellow, T. E. LaRow, S. Cocke, and J. J. O'Brien, "The role of an advanced land model in seasonal dynamical downscaling for crop model application," *J. Appl. Meteorol. Climatol.*, vol. 45, no. 5, pp. 686–701, 2006.
- [6] C. Albergel and W. Dorigo, "Monitoring multi-decadal satellite earth observation of soil moisture products through land surface reanalyses," *Remote Sens. Environ.*, vol. 138, pp. 77–89, 2013.
- [7] Y. H. Kerr, "Soil moisture from space: Where are we?" *Hydrogeol. J.*, vol. 15, no. 1, pp. 117–120, Sep. 2007.
- [8] E. G. Njoku, T. J. Jackson, L. Venkataraman, T. K. Chan, and S. V. Nghiem, "Soil moisture retrieval from AMSR-E," *IEEE Trans. Geosci. Remote Sens.*, vol. 41, no. 2, pp. 215–229, Feb. 2003.
- [9] W. Wagner, G. Lemoine, and H. Rott, "A method for estimating soil moisture from ERS scatterometer and soil data," *Remote Sens. Environ.*, vol. 70, no. 2, pp. 191–207, 1999.
- [10] T. J. Schmugge, "Remote sensing of soil moisture: Recent advances," *IEEE Trans. Geosci. Remote Sens.*, vol. GE-21, no. 3, pp. 336–344, Jul. 1983.
- [11] M. Owe, R. De Jeu, and J. Walker, "A methodology for surface soil moisture and vegetation optical depth retrieval using the microwave polarization difference index," *IEEE Trans. Geosci. Remote Sens.*, vol. 39, no. 8, pp. 1643–1654, Aug. 2001.
- [12] R. Van Der Velde, M. S. Salama, T. Pellarin, M. Ofwono, Y. Ma, and Z. Su, "Long term soil moisture mapping over the Tibetan plateau using special sensor microwave/imager," *Hydrol. Earth Syst. Sci.*, vol. 18, no. 4, pp. 1323–1337, 2014.
- [13] L. Li *et al.*, "WindSat global soil moisture retrieval and validation," *IEEE Trans. Geosci. Remote Sens.*, vol. 48, no. 5, pp. 2224–2241, May 2010.
- [14] V. Naeimi, K. Scipal, Z. Bartalis, S. Hasenauer, and W. Wagner, "An improved soil moisture retrieval algorithm for ERS and METOP scatterometer observations," *IEEE Trans. Geosci. Remote Sens.*, vol. 47, no. 7, pp. 1999–2013, Jul. 2009.
- [15] A. Chanzy *et al.*, "Airborne microwave radiometry on a semi-arid area during Hapex-Sahel," *J. Hydrol.*, vols. 188–189, pp. 285–309, 1997.
- [16] T. J. Schmugge and T. J. Jackson, "Mapping surface soil moisture with microwave radiometers," *Meteorol. Atmos. Phys.*, vol. 54, pp. 213–223, 1994.
- [17] Y. H. Kerr, P. Waldteufel, J.-P. Wigneron, J. Martinuzzi, J. Font, and M. Berger, "Soil moisture retrieval from space: The Soil Moisture and Ocean Salinity (SMOS) mission," *IEEE Trans. Geosci. Remote Sens.*, vol. 39, no. 8, pp. 1729–1735, Aug. 2001.
- [18] Y. H. Kerr *et al.*, "The SMOS soil moisture retrieval algorithm," *IEEE Trans. Geosci. Remote Sens.*, vol. 50, no. 5, pp. 1384–1403, May 2012.
- [19] T. J. Jackson *et al.*, "Vegetation water content mapping using Landsat data derived normalized difference water index for corn and soybeans," *Remote Sens. Environ.*, vol. 92, no. 4, pp. 475–482, Sep. 2004.
- [20] G. Lagerloef *et al.*, "The Aquarius/SAC-D mission: Designed to meet the salinity remote-sensing challenge," *Oceanography*, vol. 21, no. 1, pp. 68–81, 2008.
- [21] D. Entekhabi *et al.*, "The Soil Moisture Active Passive (SMAP) mission," *Proc. IEEE*, vol. 98, no. 5, pp. 704–716, May 2010.
- [22] Y. H. Kerr *et al.*, "The SMOS mission: New tool for monitoring key elements of the global water cycle," *Proc. IEEE*, vol. 98, no. 5, pp. 666–687, May 2010.
- [23] J. Wigneron *et al.*, "L-band Microwave Emission of the Biosphere (L-MEB) Model: Description and calibration against experimental data sets over crop fields," *Remote Sens. Environ.*, vol. 107, no. 4, pp. 639–655, Apr. 2007.
- [24] V. Masson, J. Champeaux, F. Chauvin, C. Meriguet, and R. Lacaze, "A global database of land surface parameters at 1-km resolution in meteorological and climate models," *J. Clim.*, vol. 16, no. 9, pp. 1261–1282, May 2003.
- [25] K. Saleh, J.-P. Wigneron, P. de Rosnay, J.-C. Calvet, and Y. Kerr, "Semi-empirical regressions at L-band applied to surface soil moisture retrievals over grass," *Remote Sens. Environ.*, vol. 101, no. 3, pp. 415–426, Apr. 2006.
- [26] H. Lawrence *et al.*, "Comparison between SMOS Vegetation Optical Depth products and MODIS vegetation indices over crop zones of the USA," *Remote Sens. Environ.*, vol. 140, pp. 396–406, Jan. 2014.
- [27] M. Parrens *et al.*, "Comparing soil moisture retrievals from SMOS and ASCAT over France," *Hydrol. Earth Syst. Sci.*, vol. 16, no. 2, pp. 423–440, Feb. 2012.
- [28] C. Mattar *et al.*, "A combined optical-microwave method to retrieve soil moisture over vegetated areas," *IEEE Trans. Geosci. Remote Sens.*, vol. 50, no. 5, pp. 1404–1413, May 2012.
- [29] P. de Rosnay *et al.*, "SMOSREX: A long term field campaign experiment for soil moisture and land surface processes remote sensing," *Remote Sens. Environ.*, vol. 102, nos. 3–4, pp. 377–389, 2006.
- [30] M. Miernecki *et al.*, "Comparison of SMOS and SMAP soil moisture retrieval approaches using tower-based radiometer data over a vineyard field," *Remote Sens. Environ.*, vol. 154, pp. 89–101, Nov. 2014.
- [31] A. R. Huete, K. Didan, T. Miura, E. P. Rodriguez, X. D. Gao, and L. G. Ferreira, "Overview of the radiometric and biophysical performance of the MODIS vegetation indices," *Remote Sens. Environ.*, vol. 83, pp. 195–213, 2002.
- [32] M. J. Brodzik and K. W. Knowles, "EASE-Grid: A versatile set of equal-area projections and grids," in *Discrete Global Grids*, M. Goodchild, Ed. Santa Barbara, CA, USA: National Center for Geographic Information & Analysis, 2002.
- [33] D. P. Dee *et al.*, "The ERA-Interim reanalysis: Configuration and performance of the data assimilation system," *Quart. J. Roy. Meteorol. Soc.*, vol. 137, no. 656, pp. 553–597, Apr. 2011.
- [34] C. Albergel *et al.*, "Evaluation of remotely sensed and modelled soil moisture products using global ground-based in situ observations," *Remote Sens. Environ.*, vol. 118, pp. 215–226, 2012.
- [35] C. Albergel *et al.*, "Skill and global trend analysis of soil moisture from reanalyses and microwave remote sensing," *J. Hydrometeorol.*, vol. 14, no. 4, pp. 1259–1277, 2013.
- [36] M. C. Hansen, R. S. DeFries, J. R. G. Townshend, and R. Sohlberg, "Global land cover classification at 1 km spatial resolution using a classification tree approach," *Int. J. Remote Sens.*, vol. 20, pp. 1331–1364, 2000.
- [37] F. T. Ulaby, R. K. Moore, and A. K. Fung, *Microwave Remote Sensing: Active and Passive, Vol. III—Volume Scattering and Emission Theory, Advanced Systems and Applications*. Norwood, MA, USA: Artech House, 1986.
- [38] T. J. Jackson, "Microwave remote sensing," *Hydrol. Process.*, vol. 7, pp. 139–152, 1993.
- [39] J.P. Wigneron *et al.*, "Soil moisture retrievals from biangular L-band passive microwave observations," *IEEE Trans. Geosci. Remote Sens.*, vol. 1, no. 4, pp. 277–281, Oct. 2004.
- [40] J. P. Wigneron, P. Waldteufel, A. Chanzy, J. C. Calvet, and Y. Kerr, "Two-dimensional microwave interferometer retrieval capabilities over land surfaces (SMOS Mission)," *Remote Sens. Environ.*, vol. 73, no. 3, pp. 270–282, 2000.
- [41] R. Rahmoune, P. Ferrazzoli, Y. H. Kerr, and P. Richaume, "SMOS level 2 retrieval algorithm over forests: Description and generation of global maps," *IEEE J. Sel. Topics Appl. Earth Observ. Remote Sens.*, vol. 6, no. 3, pp. 1430–1439, Jun. 2013.
- [42] P. Ferrazzoli, L. Guerriero, and J. P. Wigneron, "Simulating L-band emission of forests in view of future satellite applications," *IEEE Trans. Geosci. Remote Sens.*, vol. 40, no. 12, pp. 2700–2708, Dec. 2002.
- [43] M. Kurum, "Quantifying scattering albedo in microwave emission of vegetated terrain," *Remote Sens. Environ.*, vol. 129, pp. 66–74, 2013.
- [44] F. Lemaitre *et al.*, "Design and test of the ground-based L-band radiometer for estimating water in soils (LEWIS)," *IEEE Trans. Geosci. Remote Sens.*, vol. 42, no. 8, pp. 1666–1676, Aug. 2004.
- [45] K. Saleh *et al.*, "Impact of rain interception by vegetation and mulch on the L-band emission of natural grass," *Remote Sens. Environ.*, vol. 101, no. 1, pp. 127–139, Mar. 2006.
- [46] C. Albergel, L. Brocca, W. Wagner, P. de Rosnay, and J. C. Calvet, "Selection of performance metrics for global soil moisture products: The case of ASCAT product," in *Remote Sensing of Energy Fluxes and Soil Moisture Content*, G. P. Petropoulos, Ed. Boca Raton, FL, USA: CRC Press, 2013, pp. 427–443.
- [47] D. Entekhabi, R. H. Reichle, R. D. Koster, and W. T. Crow, "Performance metrics for soil moisture retrievals and application requirements," *J. Hydrometeorol.*, vol. 11, no. 3, pp. 832–840, 2010.

- [48] S. Garrigues *et al.*, "Validation and intercomparison of global Leaf Area Index products derived from remote sensing data," *J. Geophys. Res.*, vol. 113, no. G2, p. G02028, Jun. 2008.
- [49] G. Zheng and L. M. Moskal, "Retrieving Leaf Area Index (LAI) using remote sensing: Theories, methods and sensors," *Sensors*, vol. 9, no. 4, pp. 2719–2745, Jan. 2009.
- [50] C. Cassardo and N. Loglisci, "Preliminary results of an attempt to provide soil moisture datasets in order to verify numerical weather prediction models," *Nuovo Cimento*, vol. 28, no. 2, pp. 159–171, 2005.
- [51] D. J. Leroux, Y. H. Kerr, P. Richaume, and R. Fieuzaal, "Spatial distribution and possible sources of SMOS errors at the global scale," *Remote Sens. Environ.*, vol. 133, pp. 240–250, 2013.
- [52] K. Rötzer *et al.*, "Catchment scale validation of SMOS and ASCAT soil moisture products using hydrological modeling and temporal stability analysis," *J. Hydrol.*, vol. 519, pp. 934–946, Nov. 2014.
- [53] A. Pérez-Hoyos, F. J. García-Haro, and J. San-Miguel-Ayanz, "Conventional and fuzzy comparisons of large scale land cover products: Application to CORINE, GLC2000, MODIS and GlobCover in Europe," *ISPRS J. Photogramm. Remote Sens.*, vol. 74, pp. 185–201, 2012.



**Andrés Santamaría-Artigas** received the B.Sc. degree in sciences of the renewable natural resources, in 2012, and the degree in renewable natural resources engineering, in 2015, from the University of Chile, Santiago, Chile. He is a member of the Laboratory for the Analysis of the Biosphere, Department of Environmental Sciences, University of Chile. Currently, he is a Graduate Research Assistant with the Department of Geographical Sciences, University of Maryland, College Park, MD, USA. His research interests include the calibration and validation of remote sensors, radiative transfer, and data assimilation.

Mr. Santamaría-Artigas has been a participant in several national and international projects related to remote sensing such as Fondecyt-Iniciación, Fondef-IDeA, IMAGINES (FP7), MIXMOD-E, and ATAFIC 2014.



**Cristian Mattar** received the Ph.D. degree in physics from the University of Valencia, Valencia, Spain, in 2011.

He is a member of the Laboratory for Analysis of the Biosphere, Department of Environmental Sciences, University of Chile, Santiago, Chile. His research interests include optical–passive microwave remote sensing algorithms, calibration and validation test sites, spatio–temporal trends over extreme biomes, and regional water balance.

Dr. Mattar has participated in several national and international projects related to quantitative remote sensing such as Fondecyt-Iniciación, Fondef-IDeA, IMAGINES (FP7), MIXMOD-E, and international remote sensing field campaign such as DESIREX 2008, SEN3EXP 2009, THERMOPOLIS 2009, EODIX 2011, and ATAFIC 2014.



**Jean-Pierre Wigneron** (SM'03) received the M.Sc. degree in engineering from the Ecole Nationale Supérieure de l'Aéronautique et de l'Espace, Toulouse, France, in 1987, and the Ph.D. degree in remote sensing, climate and ecology from the University of Toulouse, Toulouse, in 1993.

Currently, he is a Senior Research Scientist with the Interactions Sol Plante Atmosphère (ISPA), Institut National de Recherche Agronomiques (INRA), Bordeaux, France, where he is the Coordinator of remote sensing activities at INRA and of the regional CES in Bordeaux-Aquitaine and the Head of the ISPA remote sensing team. He coordinated the development of the *L*-band Microwave Emission of the Biosphere model for soil and vegetation in the Level-2 inversion algorithm of the ESA-SMOS mission. He has authored or coauthored over 110 papers in international peer-reviewed journals. His research interests include microwave remote sensing of soil and vegetation, radiative transfer, and data assimilation.

Dr. Wigneron has been an Associate Editor of *Remote Sensing of Environment* since 2014.